

# The Impact of Model-Based Clutter Suppression on Cluttered, Aberrated Wavefronts

Kazuyuki Dei, *Student Member, IEEE*, and Brett Byram, *Member, IEEE*

**Abstract**—Recent studies reveal that both phase aberration and reverberation play a major role in degrading ultrasound image quality. We previously developed an algorithm for suppressing clutter, but we have not yet tested it in the context of aberrated wavefronts. In this paper, we evaluate our previously reported algorithm, called aperture domain model image reconstruction (ADMIRE), in the presence of phase aberration and in the presence of multipath scattering and phase aberration. We use simulations to investigate phase aberration corruption and correction in the presence of reverberation. As part of this paper, we observed that ADMIRE leads to suppressed levels of aberration. In order to accurately characterize aberrated signals of interest, we introduced an adaptive component to ADMIRE to account for aberration, referred to as adaptive ADMIRE. We then use ADMIRE, adaptive ADMIRE, and conventional filtering methods to characterize aberration profiles on *in vivo* liver data. These *in vivo* results suggest that adaptive ADMIRE could be used to better characterize a wider range of aberrated wavefronts. The aberration profiles' full-width at half-maximum of ADMIRE, adaptive ADMIRE, and postfiltered data with  $0.4\text{-mm}^{-1}$  spatial cutoff frequency are  $4.0 \pm 0.28$  mm,  $2.8 \pm 1.3$  mm, and  $2.8 \pm 0.57$  mm, respectively, while the average root-mean square values in the same order are  $16 \pm 5.4$  ns,  $20 \pm 6.3$  ns, and  $19 \pm 3.9$  ns, respectively. Finally, because ADMIRE suppresses aberration, we perform a limited evaluation of image quality using simulations and *in vivo* data to determine how ADMIRE and adaptive ADMIRE perform with and without aberration correction.

**Index Terms**—Beamforming, image quality, *in vivo*, medical ultrasound, model, phase aberration, reverberation clutter, simulation.

## I. INTRODUCTION

ULTRASOUND is a noninvasive, real-time, and affordable imaging modality that is widely used as a diagnostic tool. However, image quality can limit the usefulness of ultrasound. There are many potential causes that degrade ultrasound images, including attenuation, gross sound speed error, phase aberration, and reverberation clutter [1]–[6]. Over the past few decades, significant attention has been paid to wavefront distortion from sound speed variation throughout inhomogeneous media. The resulting degradation is primarily thought to be arrival time variation called phase aberration. In order to minimize the effects of phase aberration, many methods have been developed to correct distorted wavefronts [4], [7]–[14].

Recent studies reveal that both phase aberration and reverberation are primary contributors to degraded image

quality [5]. While phase aberration effects are caused by variations in sound speed due to tissue inhomogeneity, reverberation is caused by multiple reflections within inhomogeneous medium, generating clutter that distorts the appearance of the wavefronts from the region of interest [15]. For our purposes, we consider reverberation and multipath scattering to be identical mechanisms of clutter, because they both induce a time delay on the echo arrival time. Along with these effects, off-axis scattering, arising from scatterers located away from the beam's axis, also generates clutter and degrades image quality.

There are early studies of multipath scattering in the field of ultrasound in medicine [16]–[20]. As an example, Nicolas *et al.* [18] estimated multipath scattering *in vivo* at approximately  $-30$  dB relative to scattering signals of interest. Generally, multipath scattering was disregarded as a negligible contribution compared with the overall quality of the imaging systems at the time. However, more recent work suggests that the work on modern systems accounting for multipath scattering may be just as important as correcting aberrated wavefronts [5]. This motivated some to reconsider multipath scattering as a significant source of *in vivo* image degradation in need of new methods for correction [21]–[24]. Byram *et al.* [6], [25]–[27] introduced an aperture domain model-based algorithm that decomposes and suppresses multipath scattering and off-axis scattering, while preserving the signals of interest. This algorithm is called aperture domain model image reconstruction (ADMIRE). We can use post-ADMIRE channel data to estimate aberration profile characteristics and determine the relative contributions of reverberation and phase aberration on *in vivo* image quality.

Our motivation for this paper is to investigate phase aberration corruption and correction in the presence of reverberation within the context of our ADMIRE algorithm. ADMIRE is useful in this regard, because it can declutter the signal while preserving the channel data, which allows us to observe wavefronts before and after decluttering. As part of this, we have previously observed that ADMIRE appears to reduce the aberration in distorted wavefronts [28], but we hypothesized that it would be better to correct for aberrated wavefronts using conventional aberration correction techniques. Therefore, we introduced an adaptive component to the original ADMIRE algorithm, which we refer to as adaptive ADMIRE. The goal of adaptive ADMIRE is to more efficiently suppress clutter, while allowing the aberrated aspects of the signal from the region of interest to pass through the ADMIRE decomposition unaltered so that they can be characterized or corrected using dedicated approaches. Adaptive ADMIRE has two uses. First, it allows us to test our hypothesis regarding the best

Manuscript received July 7, 2016; accepted July 18, 2017. Date of publication July 20, 2017; date of current version October 6, 2017. This work was supported by the NIH under Grant R01EB020040 and Grant S10OD016216-01. (Corresponding author: Kazuyuki Dei.)

The authors are with the Department of Biomedical Engineering, Vanderbilt University, Nashville, TN 37235 USA (e-mail: kazuyuki.dei@vanderbilt.edu).  
Digital Object Identifier 10.1109/TUFFC.2017.2729944

way to address aberration, and second, it allows us to more accurately classify phase aberration in the presence of strong reverberation or off-axis clutter.

Here, we describe adaptive ADMIRE and use simulations to show that adaptive ADMIRE more efficiently preserves the distortions of aberrated wavefronts. Then, we use ADMIRE, adaptive ADMIRE, and conventional techniques to characterize phase aberration on *in vivo* liver data. Finally, because ADMIRE suppresses aberration, we perform a limited evaluation of image quality using simulations and *in vivo* data to determine how ADMIRE and adaptive ADMIRE perform with and without aberration correction.

## II. METHODS

### A. Aperture Domain Model Image Reconstruction

We quickly review the ADMIRE algorithm laid out by Byram *et al.* [25] to identify and suppress clutter from off-axis and multipath sources. The basic model used for the ADMIRE algorithm [25], [26] is

$$p_s(x; t, \omega) = \sum_{n=0}^{N-1} A_n(x) e^{jk\tau(x; x_n, z_n, \tau_n)}, \quad (1)$$

where  $x$  is the transducer aperture location,  $t$  and  $\omega$  are the time and frequency to localize the signal,  $k$  is the wave number,  $\tau(x; x_n, z_n, \tau_n)$  is the wavefront delay for a received signal reflecting from point  $(x_n, z_n)$  at time  $\tau_n$ , and  $N$  is the number of scatterers arriving at time  $t$ .  $A_n(x)$  is the amplitude modulation term across the transducer aperture induced by a combination of short-time Fourier transform (STFT) windowing and element sensitivity (ES)

$$A_n(x) = A_{\text{STFT}}(x) A_{\text{ES}}(x). \quad (2)$$

The first-term of (2) is

$$A_{\text{STFT}}^2(x) = \int_{t_c - \frac{\Delta t}{2}}^{t_c + \frac{\Delta t}{2}} w_{\text{STFT}}^2(t - t_c) w_{\text{env}}^2(t - \tau(x; x_n, z_n, \tau_n)) dt, \quad (3)$$

where  $\Delta t$  is the STFT window size,  $t_c$  is the middle of the STFT window,  $w_{\text{STFT}}$  is the window assigned for the STFT, and  $w_{\text{env}}$  is the axial pulse envelope function. The second-term of (2) is addressed by Selfridge *et al.* [29].

In the first step of implementing ADMIRE, dynamic receive delays are applied to RF channel data. The delayed channel data are then STFT. Next, model-fitting is performed on each frequency component of the post-STFT RF channel signals at a given depth. The model relating to the response of  $y$  can be written in the following form [25]:

$$y = X\beta, \quad (4)$$

where  $X$  is the ADMIRE model matrix for that depth and frequency, and  $\beta$  is the model coefficient vector.  $x$  and  $y$  are then expressed with the following matrices, respectively:

$$X = \begin{bmatrix} \Re\{p_s(x; t, \omega)\}^\top & -\Im\{p_s(x; t, \omega)\}^\top \\ \Im\{p_s(x; t, \omega)\}^\top & \Re\{p_s(x; t, \omega)\}^\top \end{bmatrix}, \\ y = [\Re\{S_i(mT, \omega_p)\} \quad \Im\{S_i(mT, \omega_p)\}]^\top,$$

where  $\Re$  and  $\Im$  denote the real and imaginary components, respectively,  $mT$  is the discrete time index,  $T$  is the sampling period of the RF data,  $\omega_p$  is a discrete frequency,  $S_i(mT, \omega_p)$  is the post-STFT signal for a single channel of the aperture,  $i$  indexes channel, and  $\top$  is the matrix transpose.

The goal of ADMIRE is to take the pressure,  $p_s(x; t, \omega)$ , measured by the aperture elements and solve for the right side of (1). Unfortunately, the problem is ill-posed. Therefore, the model decomposition is performed using elastic-net regularization [30]

$$\hat{\beta} = \arg \min_{\beta} (\|y - X\beta\|^2 + \lambda(\alpha\|\beta\|_1 + (1 - \alpha)\|\beta\|_2^2/2)), \quad (5)$$

where  $\|\beta\|_1$  and  $\|\beta\|_2$  denote the L1-norm and the L2-norm, respectively, and  $\alpha$  and  $\lambda$  are the parameters used for adjusting the regularization. The parameter of  $\alpha$  ranges between 0 and 1 to determine the relative weight of L1 and L2. For an elastic-net regularization solution, the degrees of freedom (DOFs) are a function of  $\lambda$  [31], given by

$$\text{DOF}(\lambda) = \text{tr}[X_A(X_A^\top X_A + \lambda I)^{-1} X_A^\top], \quad (6)$$

where  $X_A$  is the active set of the model predictors with nonzero coefficients after model-fitting with a given  $\lambda$ . (We will show that the DOFs play an important role when model mismatch from aberration is present.)

After the model-fit, model predictors within the acceptance region are used to reconstruct decluttered signals. The acceptance zone can be formulated as an ellipse, respectively, depending on the lateral and axial resolutions of  $\text{res}_{\text{lat}}$  and  $\text{res}_{\text{axl}}$

$$\left(\frac{x_n - x_r}{c_{\text{lat}} \text{res}_{\text{lat}}}\right)^2 + \left(\frac{z_n - z_r}{c_{\text{axl}} \text{res}_{\text{axl}}}\right)^2 \leq 1, \quad (7)$$

where  $x_r$  and  $z_r$  indicate the center of the acceptance zone, and  $c_{\text{lat}}$  and  $c_{\text{axl}}$  are scalable factors to adjust the acceptance region. The signal of interest (SOI) is reconstructed using

$$y_{\text{ROI}} = X_B \hat{\beta}_B, \quad (8)$$

where  $y_{\text{ROI}}$  is a decluttered signal and  $X_B$  is the model with predictors that are spatially within the acceptance zone. The decluttered signals are then converted into the original time-domain RF channel signals applying the inverse STFT [32]. Table I shows ADMIRE parameters applied for this paper.

### B. Aberration Estimation Method

We applied a multilag technique to estimate aberration profiles [33]. A window of 14 wavelengths was extracted from the data record of each channel [13]. In this method, a channel signal was compared with five neighboring channels in both directions to estimate relative time delay. The relative time delays were estimated using Loupas' 2-D autocorrelation algorithm [34].

In order to determine absolute wavefront delays, the relative delay estimates may be combined into a matrix formulation [35]

$$M\tau_{\text{aber}} = \Delta\tau_{\text{aber}}, \quad (9)$$

where  $M$  is the design matrix of channel lags,  $\tau_{\text{aber}}$  is the estimated aberration profile, and  $\Delta\tau_{\text{aber}}$  are the relative

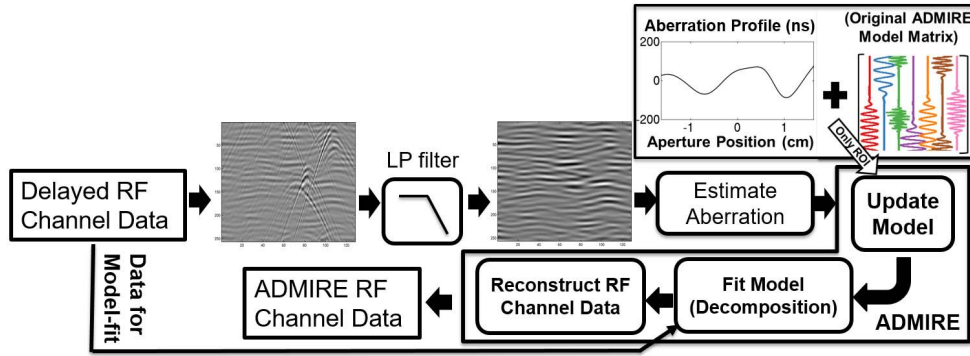


Fig. 1. Adaptive ADMIRE data flow is illustrated. Aberration profiles are estimated from the data after spatial filtering (LP filter), while the ADMIRE model-fit is applied to the unfiltered channel data. Estimated aberration profiles are used to adaptively update the original ADMIRE model.

TABLE I  
ADMIRE PARAMETERS

Parameter	Value
$\alpha$	0.9
$\lambda$	$0.0189 \sqrt{y^H y}$
$c_{lat}$	6
$c_{axl}$	2
Model space (lateral) [m]	aperture length
Model space (axial) [m]	$\{0.001, z_r + (c_{axl} res_{axl})/2\}$
Model sampling (inside) [m]	$\{0.0716 res_{lat}, 0.286 res_{axl}\}$
Model sampling (outside) [m]	$\{1.43 res_{lat}, 1.43 res_{axl}\}$
STFT window size	$(8 \log(2))/(2\pi BW f_0)$

(H is the Hermitian transpose, BW is the fractional bandwidth and  $f_0$  is the center frequency of transmitted pulse.)

time delay estimates. The estimated aberration profile,  $\tau_{aber}$ , is computed by solving the pseudoinverse matrix [33]

$$\tau_{aber} = (M^T M)^{-1} M^T \Delta \tau_{aber}. \quad (10)$$

### C. Adaptive ADMIRE

In order to enable ADMIRE to effectively preserve phase aberration while decluttering, we introduce adaptive ADMIRE so that we can address aberration directly using conventional methods. We highlight two key steps in converting ADMIRE into adaptive ADMIRE. First, we apply a spatial low-pass filter to obtain an initial estimate of aberration, and second, we adapt the ADMIRE model in the region of interest with the estimated aberration profile. Fig. 1 presents an overview of adaptive ADMIRE.

The spatial filter is applied to the delayed RF channel data before estimating the aberration profiles [36]. The filter is a low-pass filter laterally and an all-pass filter axially, leading to a 1-D spatial filter. The low-pass filter in the lateral dimension is just an  $N$ -tap finite impulse response (FIR) filter. In this paper, we applied a 20-tap zero-phase FIR filter with a spatial cutoff frequency of  $0.4 \text{ mm}^{-1}$  across the aperture dimension unless otherwise specified [36], [37]. The filter removes high-frequency spatial information, but low-frequency clutter components from reverberation persist, which is what ADMIRE addresses.

Referring to Fig. 1, aberration profiles,  $\tau_{aber}$ , which are estimated from the data after low-pass filtering, are used to adaptively update the original model around the region of interest by combining the wavefront delay,  $\tau(x; x_n, z_n, \tau_n)$ , with the estimated aberration profile

$$\tau_{adapt}(x; x_n, z_n, \tau_n) = \tau(x; x_n, z_n, \tau_n) + \tau_{aber}(x), \quad (11)$$

which also impacts the amplitude modulation term  $A_n(x)$  in (1).

To show the effect of the cutoff frequency, we performed a simulation study and then compared estimated aberration profiles from the filtered data using 0.2-, 0.4-, and  $0.6\text{-mm}^{-1}$  spatial cutoff frequencies, along with applied aberration.

### D. Simulations

To evaluate ADMIRE and adaptive ADMIRE, we performed simulation studies using Field II [38], [39] in the presence of phase aberration and in the presence of multipath scattering and phase aberration. We performed simulations for point targets positioned at 5 cm. We also simulated channel data from diffuse scatterers with a density of 25 scatterers per resolution cell to ensure fully developed speckle [40]. We modeled a linear array transducer with 3.0-MHz center frequency and 60% fractional bandwidth. Table II indicates simulated transducer parameters, including geometry.

In order to simulate the effects of aberrated wavefronts, a zero-mean, random near-field phase screen was used to model aberration profiles. The aberration model was generated by convolving a Gaussian random process with a Gaussian function [12]. The aberration model was then applied on both transmit and receive to individual mathematical subelements, making up the transducer aperture. Aberration levels were characterized by the aberration profile's autocorrelation full-width at half-maximum (FWHM) and the root-mean square (RMS). Lower autocorrelation FWHM and higher RMS are indicative of increased aberration levels. In principle, the lower autocorrelation FWHM would come from greater spatial variability in the tissues generating the aberration, whereas higher RMS would be related to larger deviations in the average sound speed relative to 1540 m/s along the path to each transducer element. We generated aberrated wavefronts of  $\text{FWHM} = 5.0 \pm 0.1 \text{ mm}$ , and  $\text{RMS} = 50 \text{ ns}$  [41],

TABLE II  
FIELD II SIMULATION PARAMETERS

Parameter	Value
Number of elements	128
Height of element	2 mm
Width of element	0.254 mm
Kerf	0.003 mm
Lateral pitch	0.257 mm
Center frequency ( $f_c$ )	3 MHz
Sampling frequency (simulation)	640 MHz
Sampling frequency (downsampled)	40 MHz
Bandwidth	60%
Transmit focal depth	5 cm
Transmit/Receive F/#	1.5

and multipath scattering was simulated using a pseudonon-linear adaptation to Field II [42], [43]. We scaled the clutter level of multipath scattering, relative to the SOI to specified signal-to-clutter ratios (SCRs)

$$\text{SCR} = 10 \log_{10} \left( \frac{P_{\text{SOI}}}{P_{\text{Clutter}}} \right). \quad (12)$$

When evaluating clutter, we considered three levels of 0-, 10-, and 20-dB SCR.

#### E. Error Metrics

We quantified aberration profile errors as a function of DOFs

$$\text{err}_{\text{aber}} = 10 \log_{10} \left( \frac{\sum (\tau_{\text{pre}} - \tau_{\text{post}})^2}{\sum \tau_{\text{pre}}^2} \right), \quad (13)$$

where  $\tau_{\text{pre}}$  is the profile estimated from the original uncluttered data, and  $\tau_{\text{post}}$  is the data after ADMIRE or adaptive ADMIRE.

We also measured FWHM and RMS percent error as a function of DOFs

$$\% \text{err}_{\text{FWHM/RMS}} = \frac{\kappa_{\text{post}} - \kappa_{\text{pre}}}{\kappa_{\text{pre}}} \times 100\%, \quad (14)$$

where  $\kappa_{\text{pre}}$  is FWHM/RMS values measured on the uncluttered wavefronts, and  $\kappa_{\text{post}}$  is measured values after ADMIRE or adaptive ADMIRE.

Along with the above-mentioned error metrics, we used a root-mean-square error (RMSE) of FWHM/RMS values quantified with aberration profiles from postfiltered and postadaptive ADMIRE data, as a function of spatial cutoff frequencies

$$\text{RMSE}_{\text{FWHM/RMS}} = \sqrt{\frac{\sum (v_{\text{post}} - v_{\text{applied}})^2}{N_{\text{rlz}}}}, \quad (15)$$

where  $v_{\text{applied}}$  are FWHM/RMS values measured on the uncluttered, unfiltered data, and  $v_{\text{post}}$  are the measured values after spatial filtering or adaptive ADMIRE, respectively.  $N_{\text{rlz}}$  is the number of realizations.

TABLE III  
*In Vivo* STUDY DESIGN

Data Measurement Parameters	
Parameter	Value
Transducer	4C-1 curvilinear array
Aperture length	3.05 cm
Center frequency ( $f_c$ )	4 MHz
Sampling frequency ( $f_s$ )	40 MHz
Speed of sound ( $c$ )	1540 m/s

#### F. *In Vivo* Studies

We measured aberration profiles on *in vivo* liver data using ADMIRE and adaptive ADMIRE. The data were obtained from a study approved by the Duke University Institutional Review Board with written consent provided by all participants. These data were acquired with a Siemens S2000 and 4C-1 curvilinear array (Siemens Healthcare, Ultrasound Business Unit, Mountain View, CA). Table III summarizes the *in vivo* data acquisition parameters.

Additionally, we computed contrast and contrast-to-noise ratio (CNR) on the B-mode images. Contrast and CNR were computed using

$$C = -20 \log_{10} \left( \frac{\mu_l}{\mu_b} \right), \quad (16)$$

and

$$\text{CNR} = 20 \log_{10} \left( \frac{|\mu_l - \mu_b|}{\sqrt{\sigma_l^2 + \sigma_b^2}} \right), \quad (17)$$

where  $(\mu_l, \sigma_l^2)$  and  $(\mu_b, \sigma_b^2)$  are the value of (mean, variance) of the enveloped but uncompressed data inside and outside hypoechoic structure, respectively.

#### G. Resolution Target and Contrast Target Simulations

Field II was used to perform resolution target simulations in the presence of phase aberration, in order to investigate and clarify the effect of ADMIRE and adaptive ADMIRE with and without aberration correction on image quality. We used the parameters in Table II for the simulations. We simulated two cases: one with resolution targets at the transmit focal depth, and the other with targets shallow to the focus. In the first case, the focal depth for transmit was fixed at a 3.0 cm depth, with an F/1.5 for transmit and receive aperture. Channel data were acquired from a simulated resolution phantom containing five point targets, located at the focal depth with lateral intervals 4, 3, 2, and 1 mm. In the second case, the scatterers were fixed, but the focus was moved to 5.0 cm. Other parameters such as F/# and frequency remained constant. We generated two sets of control data from the simulated resolution phantom with no aberration—one using standard delay-and-sum (DAS) beamforming (referred to as DAS only), and the other by applying ADMIRE.

Apart from these unaberrated data, aberrated data were also simulated. We simulated aberrators from a combination of FWHM = 5.0 and 2.5 mm and RMS = 25 and 50 ns,

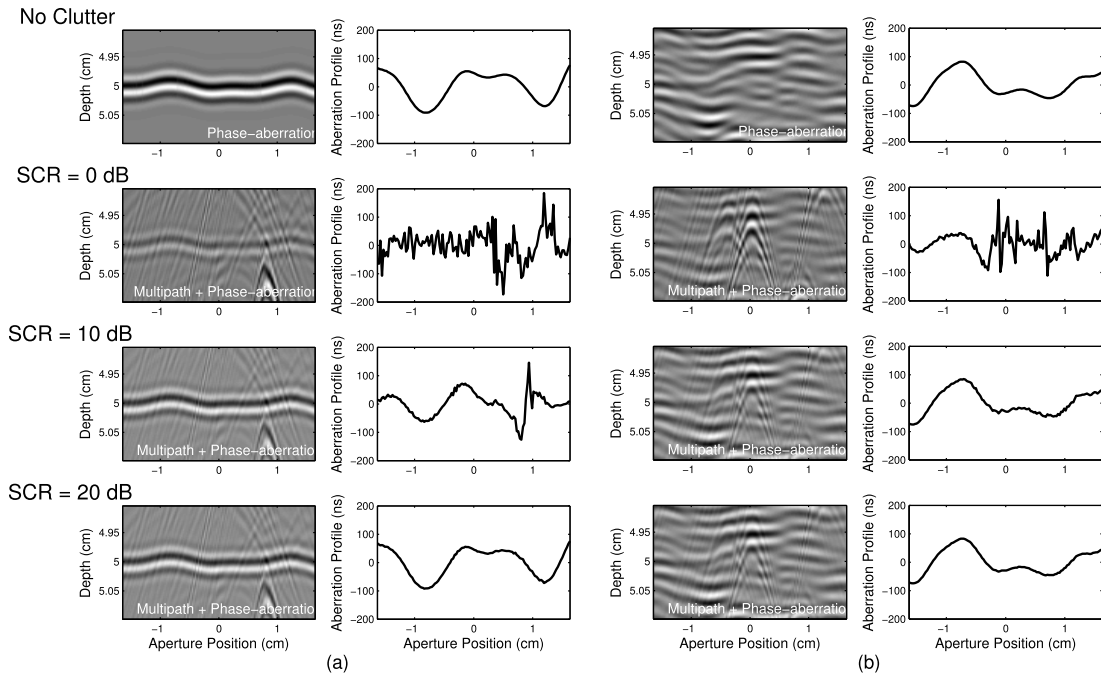


Fig. 2. Simulations in the presence of phase aberration (no clutter) and in the presence of multipath scattering and phase aberration with three different clutter levels (SCR = 0, 10, and 20 dB), having (a) a point target and (b) diffuse scattering. Four wavefronts (left) in each case of simulations, with corresponding estimated aberration profiles (right), are shown.

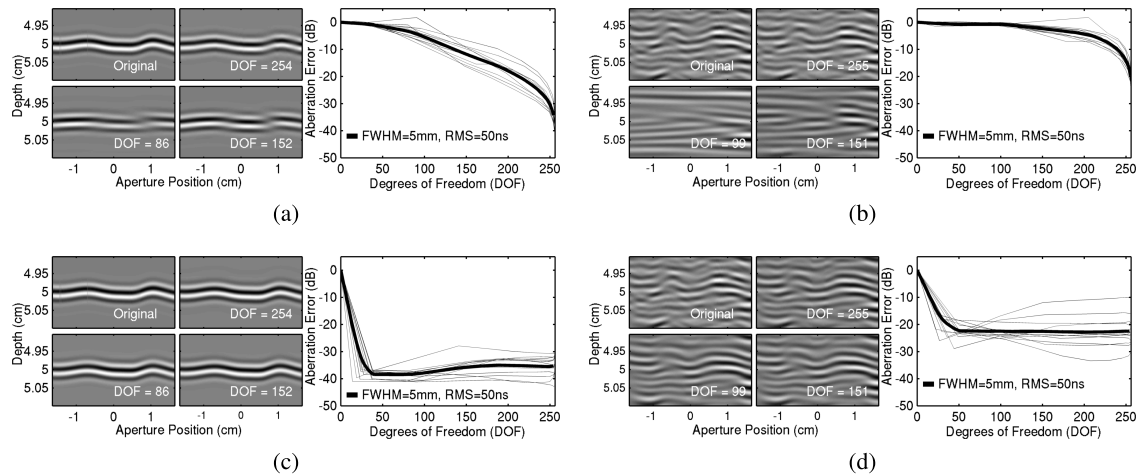


Fig. 3. Simulations in the presence of phase aberration for a point target using (a) ADMIRE and (c) adaptive ADMIRE and for diffuse scattering using (b) ADMIRE and (d) adaptive ADMIRE. Three wavefront reconstructions are shown for three different DOFs in the model-fit (left). The error of measured aberration profiles is quantified as a function of DOFs (right).

modeled as zero-mean, random near-field phase screens [12]. The selected aberrator levels were consistent with those in the literature for liver and abdominal imaging [44]–[47]. As previously described, 12 realizations were simulated for each aberrator case. We then applied normal DAS, ADMIRE, and adaptive ADMIRE with and without phase aberration correction. To implement aberration correction, we used the time-shift compensation method with estimated aberration profile for each A-line channel data at a 3.0 cm depth in a 3.6 mm window ( $4.7 \mu\text{s}$ ) [33]. Unless stated, aberration profiles are estimated from the filtered data using a spatial cutoff frequency of  $0.4 \text{ mm}^{-1}$  [36], [37].

For a metric of image quality, energy suppression was quantified with the enveloped but uncompressed B-mode data, by computing the ratio of the average intensity from adjacent point targets specified as the sum of power above  $-10 \text{ dB}$  normalized by area ( $\bar{I}_{\text{sig}}$ ) and off-axis clutter energy specified as the sum of power below  $-10 \text{ dB}$  normalized by area between the two points ( $I_{\text{clutter}}$ ), expressed by clutter ratio (CR)

$$\text{CR} = 10 \log_{10} \left( \frac{\bar{I}_{\text{sig}}}{I_{\text{clutter}}} \right). \quad (18)$$

We then determined CRs with different lateral separation lengths from DAS only and ADMIRE without aberration.

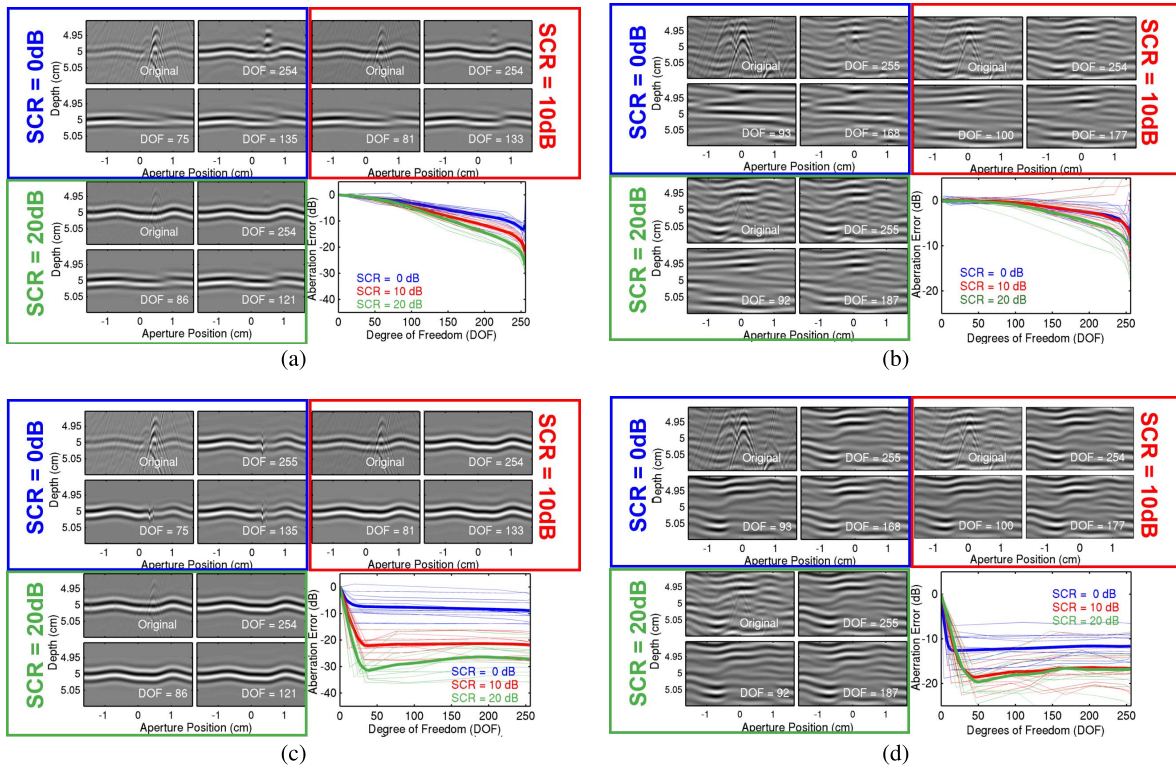


Fig. 4. Simulation in the presence of multipath scattering and phase aberration with three different clutter levels (SCR = 0, 10, and 20 dB) for a point target using (a) ADMIRE and (c) adaptive ADMIRE and for diffuse scattering using (b) ADMIRE and (d) adaptive ADMIRE. Each clutter level shows three wavefront reconstructions for three different DOFs in the model-fit. The errors of measured aberration profiles as a function of DOFs are illustrated (lower right).

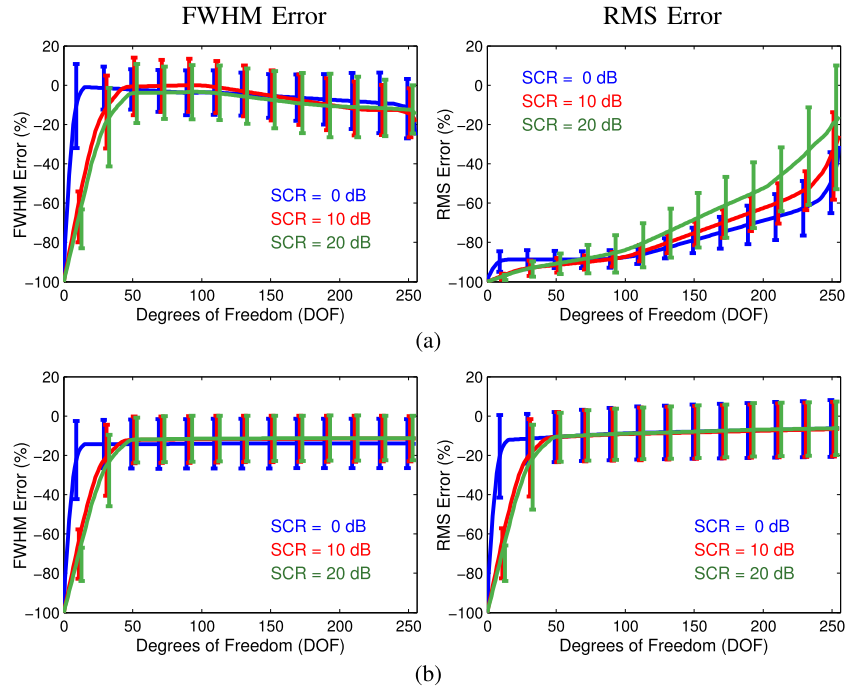


Fig. 5. FWHM (left) and RMS (right) errors from diffuse scattering simulations in the presence of multipath scattering and phase aberration with SCR = 0, 10, and 20 dB, using (a) ADMIRE and (b) adaptive ADMIRE. The aberration level is FWHM = 5.0 ± 0.1 mm and RMS = 50 ns.

We also measured the following in the presence of aberration: DAS, ADMIRE, and adaptive ADMIRE with and without aberration correction. These simulations allowed us to test whether the suppression of phase aberration using ADMIRE has a positive effect on image quality.

We also simulated anechoic cyst phantoms in Field II to further evaluate the performance of ADMIRE and adaptive ADMIRE in highly aberrated wavefronts with and without reverberation clutter. The anechoic cyst was a 5 mm diameter and 3 cm deep circle, while the background speckle was

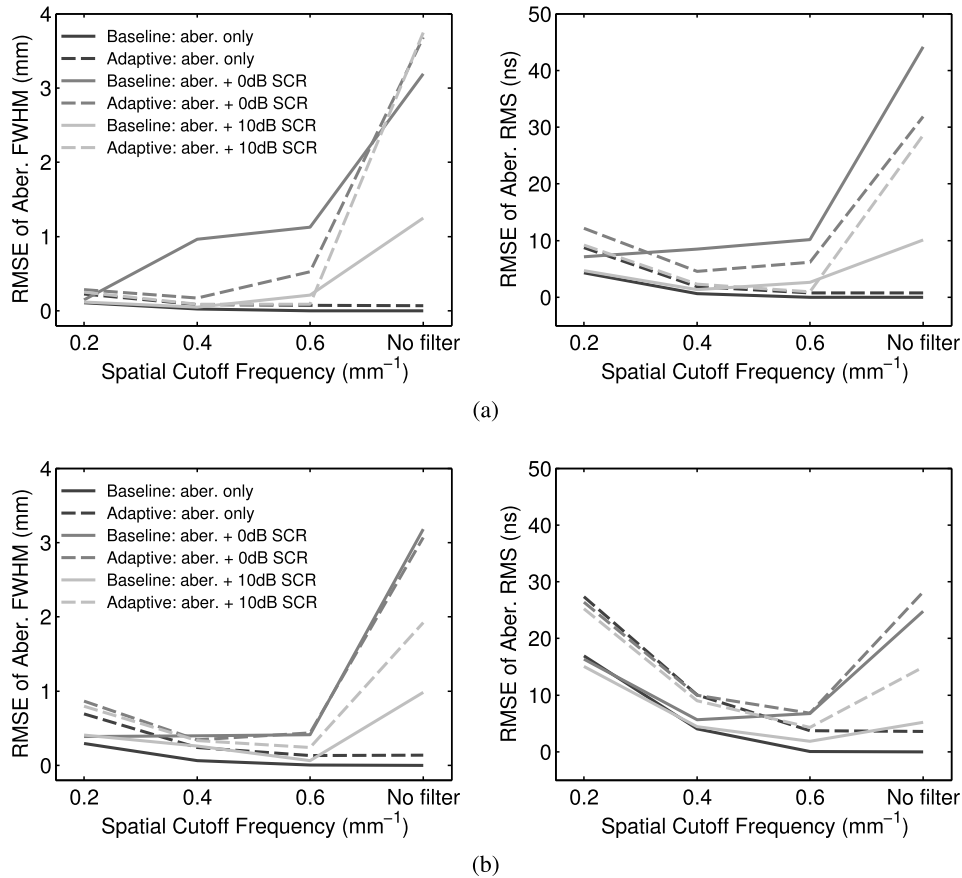


Fig. 6. RMSEs of FWHM (left) and RMS (right) quantified with aberration profiles estimated from postfilter and postadaptive ADMIRE channel data in the presence of aberration and in the presence of clutter and aberration, using (a) a point target and (b) diffuse scattering simulations. The level of aberrated wavefronts is  $\text{FWHM} = 5.0 \pm 0.1 \text{ mm}$  and  $\text{RMS} = 50 \text{ ns}$ . The RMSE values of FWHM/RMS are compared with three various spatial cutoff frequencies of 0.2, 0.4, and  $0.6 \text{ mm}^{-1}$  including an unfiltered case. The DOFs when implementing ADMIRE and adaptive ADMIRE are in a range between 50 and 70.

fully developed with a density of 25 scatterers per resolution cell [40], as indicated in Section II-D.

The aberration strength applied to this simulation was  $\text{FWHM} = 2.5 \text{ mm}$  and  $\text{RMS} = 50 \text{ ns}$ , which is modeled by a zero-mean and random near-field phase screen. We also added reverberation clutter at an SCR of 0 dB using our pseudononlinear simulation method [42]. We then performed image quality metrics—contrast and CNR measurements indicated in (16) and (17). The contrast and CNR values obtained after applying ADMIRE and adaptive ADMIRE were compared with those of DAS, respectively. We also corrected aberrated wavefronts using the same correction method we applied in resolution target simulation. We then measured contrast and CNR from aberration corrected data for DAS, ADMIRE, and adaptive ADMIRE, respectively. There are six independent speckle realizations prepared for the speckle-based target simulation.

### III. RESULTS

#### A. Aberration Profile Measurements in Simulations

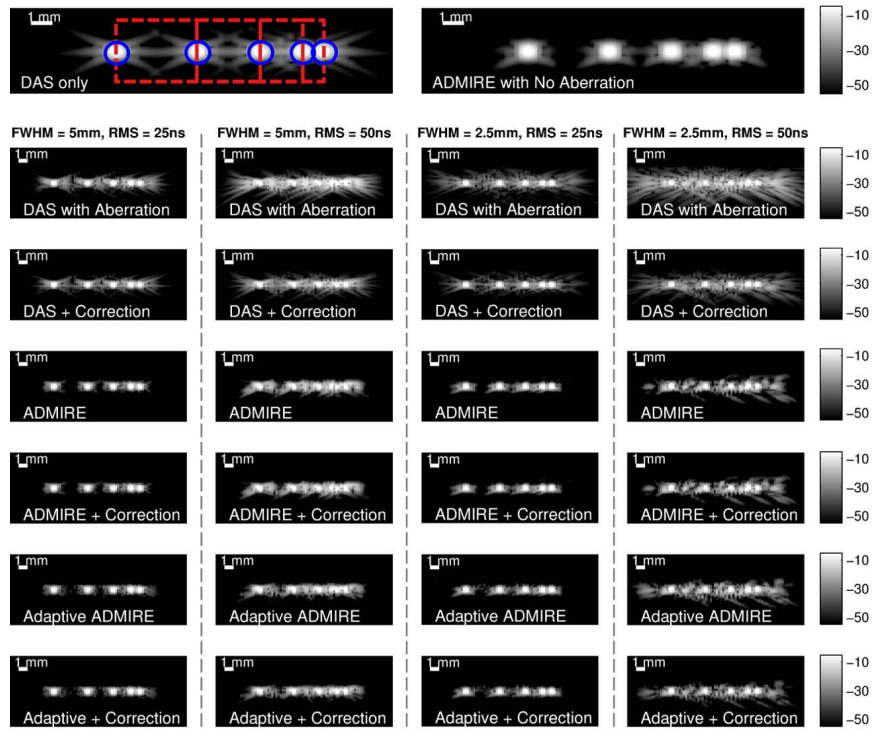
Fig. 2(a) and (b) shows two examples of wavefronts and estimated aberration profiles from a point target and diffuse scattering simulations in the presence of phase aberration and in the presence of multipath scattering and phase aberration. The results suggest that reverberation clutter could distort the

appearance of wavefronts from the region of interest. Both estimated aberration profiles with 0 and 10 dB signal-to-SCRs were distorted in the point target and diffuse scattering simulations. Aberration profiles in simulations with a lower clutter level ( $\text{SCR} = 20 \text{ dB}$ ) are comparable to cases without additional clutter. These results reveal how multipath scattering could impact aberration profile measurements.

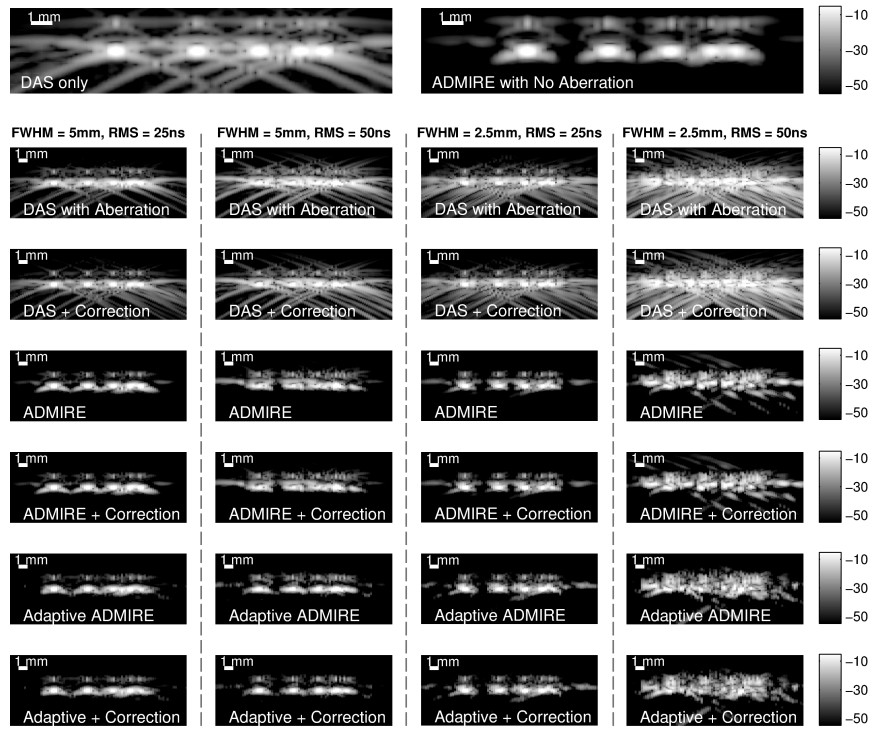
#### B. Aberration Profile Errors From Simulations

Figs. 3 and 4 show measured aberration profile errors, including wavefront reconstructions for three different DOFs for the ADMIRE decomposition. Fig. 3 shows the first set of results. The first set of results from a point target and diffuse scattering simulations derived from ADMIRE and adaptive ADMIRE in the presence of phase aberration are shown. Results in Fig. 3(a) and (b) suggest that ADMIRE suppresses phase aberration when the DOFs are low. In contrast, Fig. 3(b) and (d) shows that adaptive ADMIRE preserves phase aberration-based wavefront distortion even at low DOFs indicating that adaptive ADMIRE produces a more parsimonious model in the presence of phase aberration, meaning that the model produces a better fit with fewer DOFs.

Fig. 4 shows a point target and diffuse scattering simulations, using ADMIRE and adaptive ADMIRE, in the



(a)



(b)

Fig. 7. Simulated wire phantom images on resolution target simulations are presented. Four blue circles are the areas used to measure power of enveloped signal, while four sections enclosed by the red dashed lines are the areas used to measure off-axis clutter energy, for lateral separation intervals of 4, 3, 2, and 1 mm, respectively. Two images on the top row with different aberrator strengths at (a) focus at the target depth and (b) focus past the target depth are also shown.

presence of multipath scattering and phase aberration. Fig. 4 qualitatively demonstrates that ADMIRE and adaptive ADMIRE suppress most clutter. Fig. 4(b) and (d) also shows

that adaptive ADMIRE better preserves phase aberration in the presence of multipath scattering, because aberration errors converge with lower DOFs. These findings suggest that

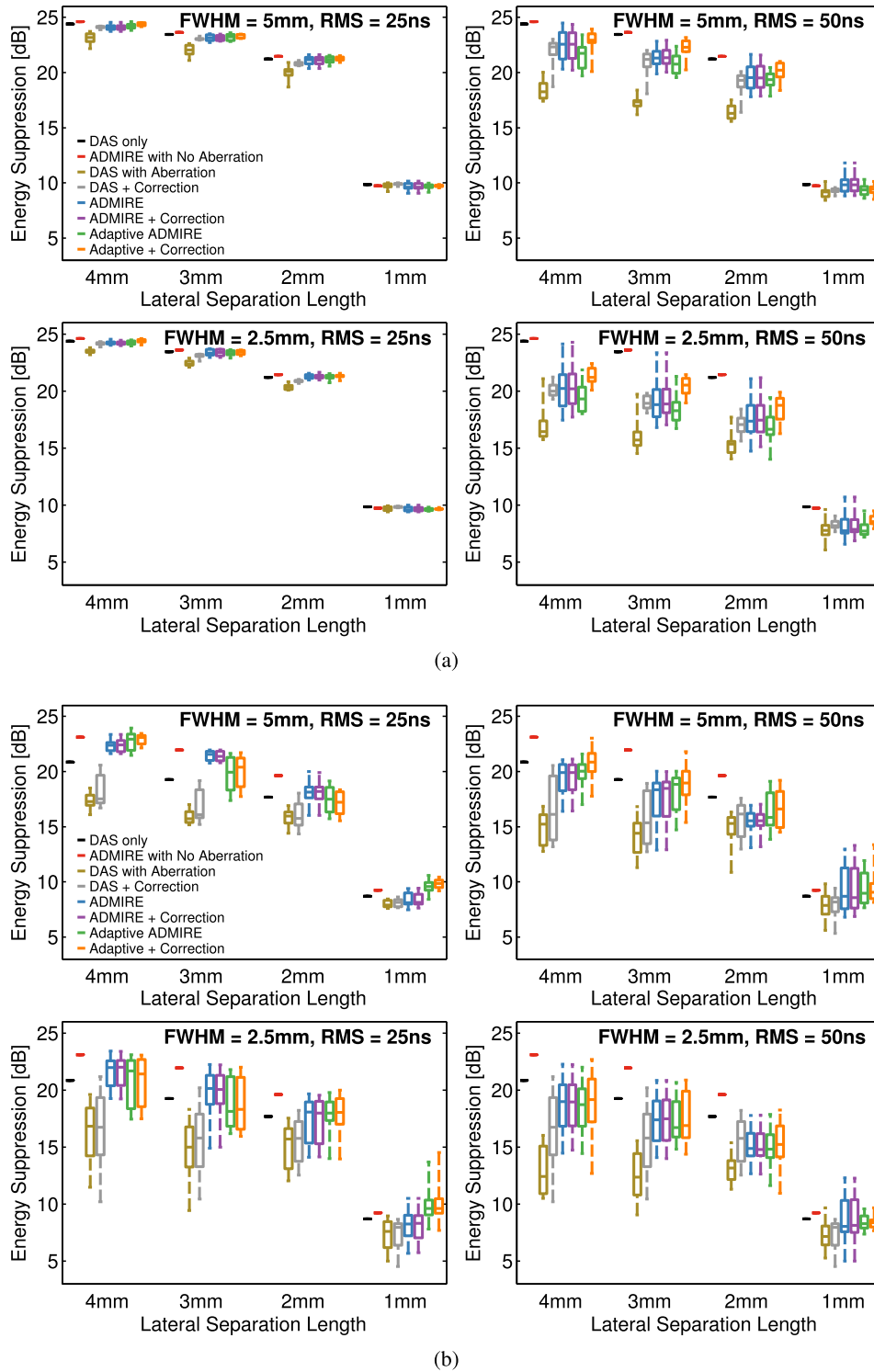


Fig. 8. Results of measured energy suppression for several lateral separation lengths are shown as boxplots, including four sets of different aberration levels. Each set of results from the cases at (a) focus at the target depth and (b) focus past the target depth includes DAS only, ADMIRE with no aberration, 12 realizations for DAS with aberration, post-ADMIRE, and postadaptive ADMIRE with and without phase aberration correction applied. Aberration profiles are estimated from the filtered data using a spatial cutoff frequency of  $0.4 \text{ mm}^{-1}$ .

adaptive ADMIRE enables us to better characterize reverberation clutter effects and phase aberration by separating these two effects.

Comparing results from a point target and diffuse scattering simulations in the presence of phase aberration (Fig. 3) and in the presence of multipath scattering and phase aberration (Fig. 4) shows that aberration profiles estimated from

diffuse scatterers have larger errors than those in a point target with the same DOFs.

### C. FWHM and RMS Errors From Simulations

Fig. 5 shows the results from diffuse scattering simulations in the presence of multipath scattering and phase aberration, using (a) ADMIRE and (b) adaptive ADMIRE.

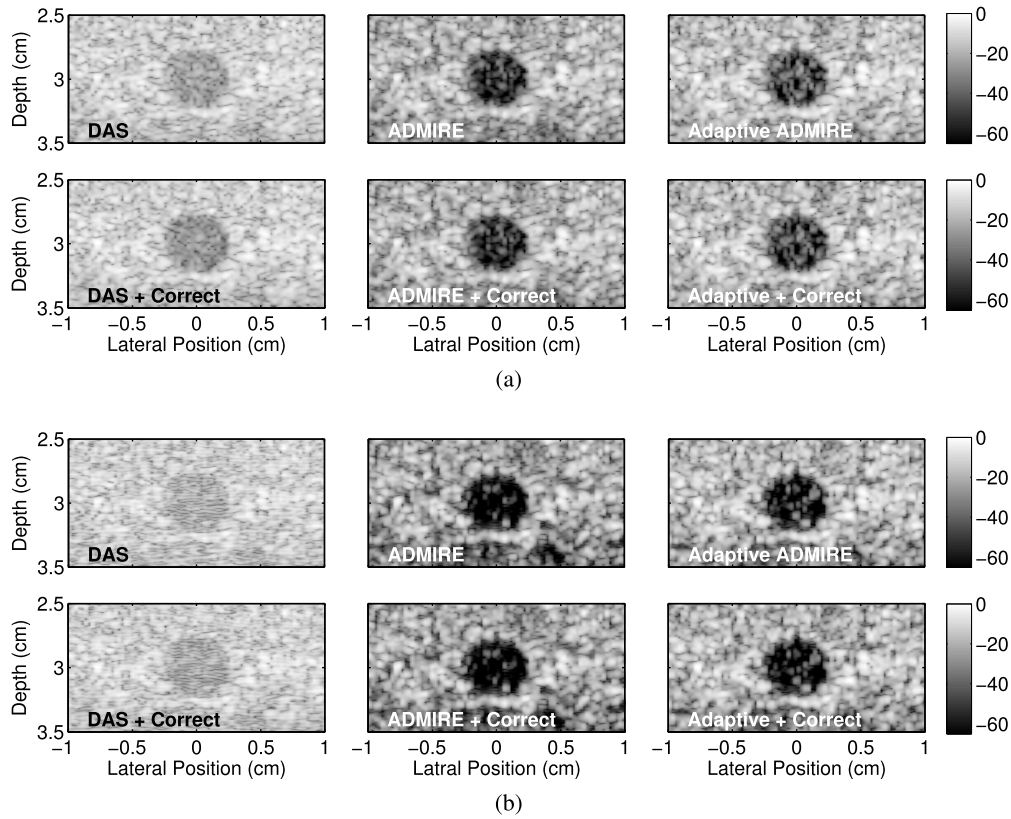


Fig. 9. Matched simulated anechoic cyst phantom images formed after applying DAS, ADMIRE, and adaptive ADMIRE with and without aberration correction in the presence of aberrated wavefronts with  $\text{FWHM} = 2.5$  mm and  $\text{RMS} = 50$  ns strength, in the cases of (a) uncluttered and (b)  $\text{SCR} = 0$  dB cluttered environments, respectively.

Comparing the results of RMS errors, the RMS errors resulting from adaptive ADMIRE decrease and converge quickly with lower DOFs, relative to ADMIRE. These results indicate that ADMIRE does not efficiently reproduce aberrated wavefronts with low DOFs, while adaptive ADMIRE reasonably preserves the phase aberration profile. These findings are consistent with those observed with the aberration profile errors.

#### D. Root-Mean-Square Errors of FWHM and RMS From Simulations

Fig. 6 shows the results of computing RMSE of aberration profiles' FWHM and RMS values, from several different scenarios, as a function of three spatial filter cutoffs including an unfiltered case. These scenarios included aberrated wavefronts that are uncluttered, and aberrated wavefronts that are cluttered with 0 and 10 dB SCR, but not including 20 dB SCR case because of minimal differences from the uncluttered case. The results of spatial filtering are consistent with the literature [36], [37]. We also observe that spatial cutoff frequencies of  $0.4$  and  $0.6$   $\text{mm}^{-1}$  may not make much of a difference in the presence of moderate clutter when comparing wavefronts obtained after filtering and adaptive ADMIRE. These findings suggest that adaptive ADMIRE is effective in preserving the distortion of aberrated wavefronts in the presence of strong clutter environments, in conjunction with spatial filtering with appropriate cutoff frequencies.

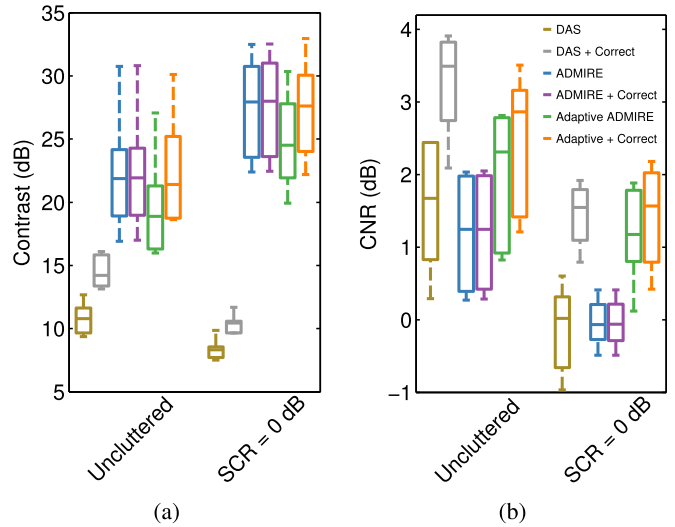


Fig. 10. Results of simulated anechoic cyst image quality metrics quantifying (a) contrast and (b) CNR for uncluttered and  $\text{SCR} = 0$  dB clutter scenarios, respectively. There are six independent speckle realizations prepared for this simulation.

#### E. Energy Suppression From Resolution Simulations

Because we observed that ADMIRE leads to suppressed levels of aberration, we report some simple results related to image quality. Figs. 7 and 8 show the simulated resolution phantom and the measured energy suppression with

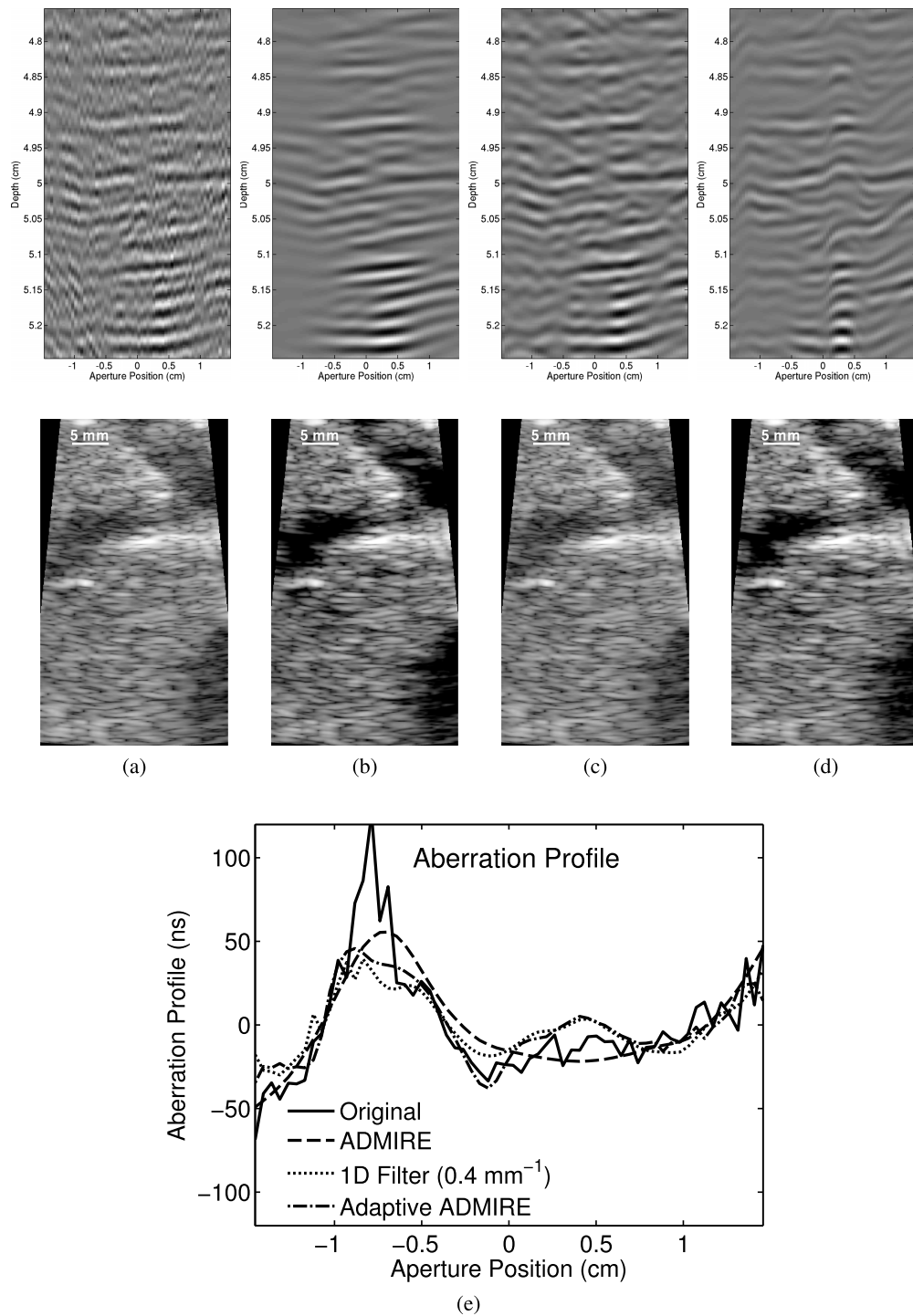


Fig. 11. Wavefronts and corresponding B-mode images of (a) original *in vivo* data, (b) ADMIRE, (c) 1-D Filter ( $0.4 \text{ mm}^{-1}$  cutoff), and (d) adaptive ADMIRE are shown, along with (e) corresponding estimated aberration profiles. The results indicate that ADMIRE, specifically, appears to smooth the wavefront and suppresses aberration while adaptive ADMIRE seems to preserve aberration so it can be characterized more accurately.

four lateral separation intervals and four sets of different aberration levels at focus at the target depth and (b) focus past the target depth. The simulated data include DAS only, ADMIRE with no aberration, 12 realizations for DAS with aberration, post-ADMIRE, and postadaptive ADMIRE with and without phase aberration correction at focus at the target depth and focus past the target depth, respectively. The simulations reveal

several points. First, as expected, phase aberration lowers spatial resolution and degrades image quality due to higher side lobes. Second, phase aberration correction applied to post-ADMIRE data provides little additional improvement, while DAS and postadaptive ADMIRE with aberration correction show some improvement, particularly in the cases with higher aberration levels. Finally, adaptive ADMIRE plus aberration

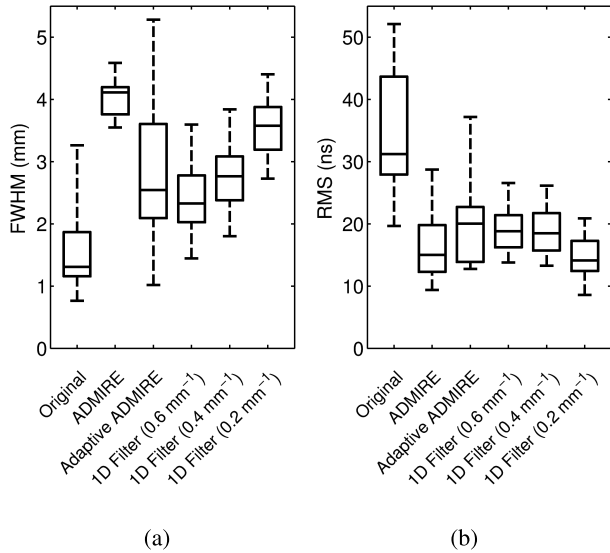


Fig. 12. Results of characterization of estimated aberration profiles from *in vivo* data are shown as boxplots. Results are shown for the original *in vivo* data, post-ADMIRE, postadaptive ADMIRE, and postfiltered data with three various spatial cutoff frequencies (0.6, 0.4, and 0.2 mm<sup>-1</sup>). Aberration profiles are characterized by (a) autocorrelation length FWHM and (b) RMS.

correction has the most benefit on image quality when the targets are close and at the focus. The results also indicate that the suppression of phase aberration as a result of ADMIRE is useful and beneficial to image quality improvement, but these results are most compelling when targets are far apart.

#### F. Simulated Anechoic Cyst Image Quality

Along with the resolution target simulation, we performed contrast target simulations. Fig. 9 demonstrates the matched simulated anechoic cyst phantom images formed after applying DAS, ADMIRE, and adaptive ADMIRE, with and without aberration correction. When compared with DAS images, ADMIRE and adaptive ADMIRE recover image quality and provide better contrast in and around the cyst region, suppressing image degradation sources (i.e., clutter). Accounting for images after applying aberration correction method, there is no significant improvement before and after correction with qualitative measures, but we still identify small improvement in background speckle patterns in the cases of DAS and adaptive ADMIRE.

To quantify the image data in Fig. 9, we computed the values of contrast and CNR, as reported in Fig. 10. In the case of DAS with uncluttered and SCR 0 dB clutter environments, aberration correction significantly improves image quality, particularly in CNR. In principle, since adaptive ADMIRE preserves phase aberration during decluttering, we observe that ADMIRE images may have higher contrast than the images formed after applying adaptive ADMIRE, but aberration correction processed after adaptive ADMIRE may recover degraded image quality caused by wavefront distortion. Results obtained from adaptive ADMIRE with aberration correction indicates image quality improvement in contrast and CNR when compared with those values of adaptive ADMIRE. It is also interesting to note that ADMIRE and adaptive

TABLE IV  
RELATIVE IMPROVEMENT FROM ORIGINAL B-MODE (*In Vivo*)

Algorithm	Contrast Improvement (dB)	CNR Improvement (dB)
Aberration Correction	0.090 ± 0.27	0.076 ± 0.23
ADMIRE	7.1 ± 2.5	0.86 ± 0.92
ADMIRE+Correction	6.8 ± 2.3	0.90 ± 0.89
Adaptive ADMIRE	6.6 ± 2.7	0.87 ± 1.1
Adaptive+Correction	6.5 ± 2.7	0.72 ± 1.1

ADMIRE may be more robust in the presence of higher clutter environments, together with higher aberrated wavefronts. Additionally, these findings from the contrast target simulations are consistent with the resolution target simulation results in Fig. 8.

#### G. Characterization of Aberration Profiles From *In Vivo* Data

We used 13 sets of *in vivo* liver data to characterize aberration profiles. The aberration profiles' FWHM and RMS were quantified. Fig. 11 demonstrates wavefronts and B-mode images obtained from one example case and the matched data after applying ADMIRE, 1-D spatial filter (0.4 mm<sup>-1</sup> cutoff), and adaptive ADMIRE, along with the corresponding estimated aberration profiles. The results indicate that ADMIRE smooths the aberrated wavefronts and suppresses aberration, compared with the wavefronts obtained from postadaptive ADMIRE data. It is also worth noting that the resulting B-mode images from ADMIRE and adaptive ADMIRE are qualitatively better than other images obtained from the original *in vivo* data and the postfiltered data.

Fig. 12 demonstrates effect of the spatial filter on *in vivo* data. Low cutoff frequencies may remove aberrated signals containing high spatial frequency components along with clutter; while aberration estimation may be less accurate when using high cutoff frequencies due to unsuppressed off-axis or reverberation clutter corrupting aberration measurements. Fig. 12 also indicates that there is potential for significant bias based on the spatial filter that is chosen. This trend is particularly noticeable in Fig. 12(a). However, with adaptive ADMIRE, which only uses the spatial filters as an initial estimate of the aberration profile, we observe that adaptive ADMIRE has a much wider range of estimated aberration levels. These *in vivo* results highlight a shortcoming of conventional method and demonstrate the potential role of adaptive ADMIRE for better characterizing aberrated wavefronts when there is little prior knowledge of the degree of wavefront distortion.

#### H. *In Vivo* Image Quality

We compare three algorithms—aberration correction, ADMIRE, and adaptive ADMIRE. The aberration correction method was applied to post-ADMIRE and postadaptive ADMIRE data. Results, as shown in Fig. 13, demonstrate that ADMIRE and adaptive ADMIRE improved both contrast and CNR from normal B-mode images. Table IV also summarizes the relative improvements of the contrast and CNR.

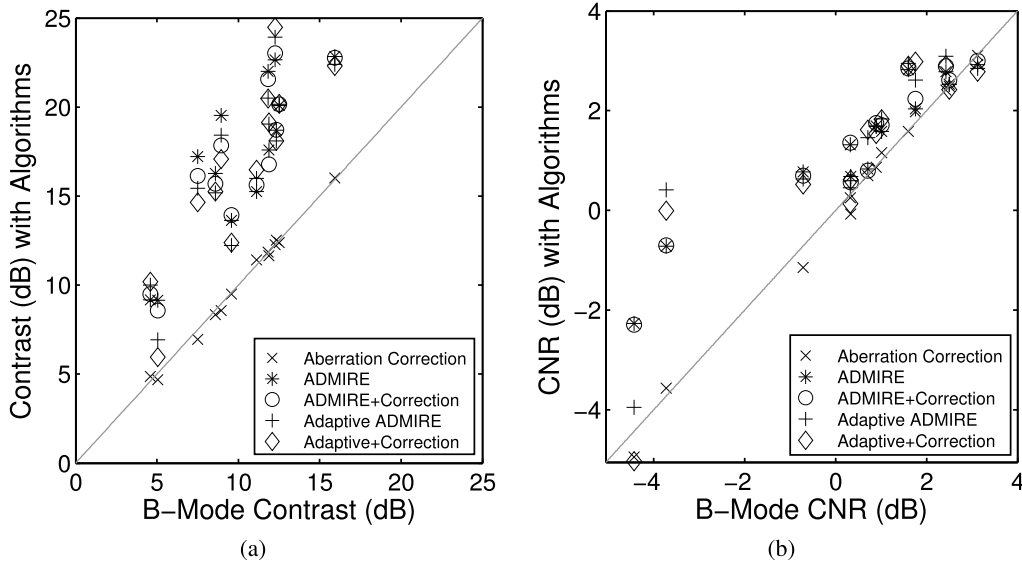


Fig. 13. Contrast and CNR with algorithms are plotted as a function of contrast and CNR of the normal B-mode image. There are 13 contrast and CNR measurements obtained from each algorithm. (a) Contrast. (b) CNR.

These results may be based on ADMIRE, because anechoic regions visible in normal B-mode were used to quantify image quality.

#### IV. DISCUSSION AND CONCLUSION

Here we considered the role of model-based methods in the presence of aberration. The results show that ADMIRE only preserves phase aberration when the DOFs are high. To make the model more parsimonious in the presence of aberration, we introduced adaptive ADMIRE.

Simulations that included both multipath scattering and phase aberration showed that multipath scattering distorts estimates of wavefront aberration, as shown in Fig. 2. Specifically, aberration levels in the presence of clutter are estimated to be higher than the simulated level of aberration.

We then evaluated ADMIRE and adaptive ADMIRE performance *in vivo*, quantifying aberration profiles. The results, as shown in Figs. 7 and 8, highlight a shortcoming of conventional filters and demonstrate the potential role of adaptive ADMIRE for better charactering aberrated wavefronts when there is little prior knowledge of the degree of wavefront distortion. These *in vivo* data results are restricted to abdominal imaging and are consistent with related literature [44], and it is known that levels of aberration are different in other scenarios like breast imaging and echocardiography. Additionally, in this paper, we applied aberration estimation and correction methods that are simple and basic with fundamental limitations [48]. It is possible that more sophisticated algorithms may yield better results.

As stated previously, adaptive ADMIRE has two major aims. The first aim is to establish a tool to test the best way to address aberration, while the second aim is to effectively differentiate aberrated signals of interest from other forms of clutter, and these aberrations are well addressed by aberration correction methods. Based on the findings

from simulations, adaptive ADMIRE shows an ability to preserve aberration while decluttering. For instance, results in Figs. 4 and 5 demonstrate that adaptive ADMIRE can reproduce original aberrated wavefronts with very low DOFs, compared with ADMIRE. Fig. 6 also reveals that adaptive ADMIRE can identify phase aberration effects in the presence of clutter and aberration. These results indicate that adaptive ADMIRE may be useful to accomplish the second aim. However, to increase performance, adaptive ADMIRE should be implemented with a suitable spatial filter. One possible explanation for the benefit seen by ADMIRE and adaptive ADMIRE is the reduction of aberrator integration error after reconstruction.

Finally, we briefly examined the role that ADMIRE and adaptive ADMIRE play on image quality in the presence of wavefront aberration. The results in Figs. 8 and 10 suggest that ADMIRE plus aberration correction does not provide any additional improvement, but that use of adaptive ADMIRE followed by conventional aberration estimation and correction methods could be the best way to address aberration effects when targets are at the focus. The suggested approach may be more effective in higher aberrated environments, as shown in Fig. 8 with FWHM = 2.5 mm, RMS = 50 ns, and FWHM = 5 mm, RMS = 50 ns. The findings are also indicated in the speckle-based target simulation results shown in Fig. 10, while the image quality metrics show that contrast in images obtained from ADMIRE with and without correction is similar to the image contrast from adaptive ADMIRE plus correction, but the ADMIRE CNR values are lower than those of adaptive ADMIRE plus correction. A possible explanation for this may be that we selected low DOFs when implementing ADMIRE with model-mismatch due to local sound speed variation (i.e., phase aberration). ADMIRE with higher DOFs loses contrast but increases CNR. The *in vivo* results (Fig. 13) are consistent with those of simulations, because most of the features of

interest *in vivo* images may be outside of the transmit focus' depth of field, but in some cases, adaptive ADMIRE plus correction improves contrast and CNR compared with adaptive ADMIRE. The image quality results also demonstrate that ADMIRE by itself suppresses phase aberration effects along with clutter, providing benefits to image quality compared with conventional methods.

#### ACKNOWLEDGMENT

The authors would like to thank the staff of the Vanderbilt University ACCRE computing resource. They would also like to thank J. Dahl for insightful suggestions.

#### REFERENCES

- [1] J. T. Bushberg and J. M. Boone, *The Essential Physics of Medical Imaging*. Baltimore, MD, USA: Williams & Wilkins, 2011.
- [2] M. E. Anderson and G. E. Trahey, "The direct estimation of sound speed using pulse-echo ultrasound," *J. Acoust. Soc. Amer.*, vol. 104, no. 5, pp. 3099–3106, 1998.
- [3] M. Anderson, M. McKeag, and G. Trahey, "The impact of sound speed errors on medical ultrasound imaging," *J. Acoust. Soc. Amer.*, vol. 107, no. 6, pp. 3540–3548, 2000.
- [4] S. Flax and M. O'Donnell, "Phase-aberration correction using signals from point reflectors and diffuse scatterers: Basic principles," *IEEE Trans. Ultrason., Ferroelect., Freq. Control*, vol. 35, no. 6, pp. 758–767, Jun. 1988.
- [5] G. F. Pinton, G. E. Trahey, and J. J. Dahl, "Sources of image degradation in fundamental and harmonic ultrasound imaging using nonlinear, full-wave simulations," *IEEE Trans. Ultrason., Ferroelect., Freq. Control*, vol. 58, no. 6, pp. 1272–1283, Jun. 2011.
- [6] B. Byram and M. Jakovljevic, "Ultrasonic multipath and beamforming clutter reduction: A chirp model approach," *IEEE Trans. Ultrason., Ferroelect., Freq. Control*, vol. 61, no. 3, pp. 428–440, Mar. 2014.
- [7] M. O'Donnell and S. Flax, "Phase aberration measurements in medical ultrasound: Human studies," *Ultrason. Imag.*, vol. 10, no. 1, pp. 1–11, 1988.
- [8] M. Karaman, A. Atalar, H. Köymen, and M. O'Donnell, "A phase aberration correction method for ultrasound imaging," *IEEE Trans. Ultrason., Ferroelect., Freq. Control*, vol. 40, no. 4, pp. 275–282, Apr. 1993.
- [9] D. L. Liu and R. C. Waag, "Correction of ultrasonic wavefront distortion using backpropagation and a reference waveform method for time-shift compensation," *J. Acoust. Soc. Amer.*, vol. 96, no. 2, pp. 649–660, 1994.
- [10] L. M. Hinkelman, D.-L. Liu, R. C. Waag, Q. Zhu, and B. D. Steinberg, "Measurement and correction of ultrasonic pulse distortion produced by the human breast," *J. Acoust. Soc. Amer.*, vol. 97, no. 3, pp. 1958–1969, 1995.
- [11] M. Tabei, T. D. Mast, and R. C. Waag, "Simulation of ultrasonic focus aberration and correction through human tissue," *J. Acoust. Soc. Amer.*, vol. 113, no. 2, pp. 1166–1176, 2003.
- [12] J. J. Dahl, D. A. Guenther, and G. E. Trahey, "Adaptive imaging and spatial compounding in the presence of aberration," *IEEE Trans. Ultrason., Ferroelect., Freq. Control*, vol. 52, no. 7, pp. 1131–1144, Jul. 2005.
- [13] J. J. Dahl, S. A. Mcleavey, G. F. Pinton, M. S. Soo, and G. E. Trahey, "Adaptive imaging on a diagnostic ultrasound scanner at quasi real-time rates," *IEEE Trans. Ultrason., Ferroelect., Freq. Control*, vol. 53, no. 10, pp. 1832–1843, Oct. 2006.
- [14] J. C. Tillett, J. P. Astheimer, and R. C. Waag, "A model of distributed phase aberration for deblurring phase estimated from scattering," *IEEE Trans. Ultrason., Ferroelect., Freq. Control*, vol. 57, no. 1, pp. 214–228, Jan. 2010.
- [15] J. J. Dahl and N. M. Sheth, "Reverberation clutter from subcutaneous tissue layers: Simulation and *in vivo* demonstrations," *Ultrasound Med. Biol.*, vol. 40, no. 4, pp. 714–726, 2014.
- [16] L. L. Foldy, "The multiple scattering of waves. I. General theory of isotropic scattering by randomly distributed scatterers," *Phys. Rev.*, vol. 67, nos. 3–4, p. 107, 1945.
- [17] R. Chivers, "The scattering of ultrasound by human tissues—Some theoretical models," *Ultrasound Med. Biol.*, vol. 3, no. 1, pp. 1–13, 1977.
- [18] D. Nicholas, C. Hill, and D. Nassiri, "Evaluation of backscattering coefficients for excised human tissues: Principles and techniques," *Ultrasound Med. Biol.*, vol. 8, no. 1, pp. 7–15, 1982.
- [19] D. Nicholas, "Evaluation of backscattering coefficients for excised human tissues: Results, interpretation and associated measurements," *Ultrasound Med. Biol.*, vol. 8, no. 1, pp. 17–28, 1982.
- [20] S. Bly, F. Foster, M. Patterson, D. Foster, and J. Hunt, "Artifactual echoes in *B*-mode images due to multiple scattering," *Ultrasound Med. Biol.*, vol. 11, no. 1, pp. 99–111, 1985.
- [21] M. Fink, "Time reversal of ultrasonic fields. I. Basic principles," *IEEE Trans. Ultrason., Ferroelect., Freq. Control*, vol. 39, no. 5, pp. 555–566, Sep. 1992.
- [22] M. A. Lediju, M. J. Pihl, J. J. Dahl, and G. E. Trahey, "Quantitative assessment of the magnitude, impact and spatial extent of ultrasonic clutter," *Ultrason. Imag.*, vol. 30, no. 3, pp. 151–168, 2008.
- [23] J. J. Dahl, M. Jakovljevic, G. F. Pinton, and G. E. Trahey, "Harmonic spatial coherence imaging: An ultrasonic imaging method based on backscatter coherence," *IEEE Trans. Ultrason., Ferroelect., Freq. Control*, vol. 59, no. 4, pp. 648–659, Apr. 2012.
- [24] S. P. Nasholm and B. A. Angelsen, "Surf imaging beams in an aberrative medium: Generation and postprocessing enhancement," *IEEE Trans. Ultrason., Ferroelect., Freq. Control*, vol. 59, no. 11, pp. 2588–2595, Nov. 2012.
- [25] B. Byram, K. Dei, J. Tierney, and D. Dumont, "A model and regularization scheme for ultrasonic beamforming clutter reduction," *IEEE Trans. Ultrason., Ferroelect., Freq. Control*, vol. 62, no. 11, pp. 1913–1927, Nov. 2015.
- [26] B. Byram, K. Dei, and D. Dumont, "An improved acoustic clutter model and direct *in vivo* assessment of off-axis and multipath clutter energy in the liver," in *Proc. IEEE Int. Ultrason. Symp. (IUS)*, Sep. 2014, pp. 531–534.
- [27] B. Byram, "Ultrasonic reverberation and off-axis clutter suppression using aperture domain signal decomposition," *Proc. SPIE*, vol. 8675, p. 86750T, Mar. 2013.
- [28] K. Dei and B. Byram, "Model-based clutter suppression in the presence of phase-aberration from *in vivo* data and simulations," in *Proc. IEEE Int. Ultrason. Symp. (IUS)*, Oct. 2015, pp. 1–4.
- [29] A. Selfridge, G. Kino, and B. Khuri-Yakub, "A theory for the radiation pattern of a narrow-strip acoustic transducer," *Appl. Phys. Lett.*, vol. 37, no. 1, pp. 35–36, 1980.
- [30] H. Zou and T. Hastie, "Regularization and variable selection via the elastic net," *J. Roy. Statist. Soc., B (Statistical Methodology)*, vol. 67, no. 2, pp. 301–320, 2005.
- [31] R. J. Tibshirani and J. Taylor, "Degrees of freedom in lasso problems," *Ann. Statist.*, vol. 40, no. 2, pp. 1198–1232, 2012.
- [32] B. Yang, "A study of inverse short-time Fourier transform," in *Proc. IEEE Int. Conf. Acoust., Speech Signal Process.*, Apr. 2008, pp. 3541–3544.
- [33] D. L. Liu and R. C. Waag, "Time-shift compensation of ultrasonic pulse focus degradation using least-mean-square error estimates of arrival time," *J. Acoust. Soc. Amer.*, vol. 95, no. 1, pp. 542–555, 1994.
- [34] T. Loupas, J. T. Powers, and R. W. Gill, "An axial velocity estimator for ultrasound blood flow imaging, based on a full evaluation of the Doppler equation by means of a two-dimensional autocorrelation approach," *IEEE Trans. Ultrason., Ferroelect., Freq. Control*, vol. 42, no. 4, pp. 672–688, Jul. 1995.
- [35] R. C. Gauss, G. E. Trahey, and M. S. Soo, "Wavefront estimation in the human breast," *Proc. SPIE*, vol. 4325, pp. 172–181, May 2001.
- [36] J. J. Dahl and T. J. Feehan, "Direction of arrival filters for improved aberration estimation," *Ultrason. Imag.*, vol. 30, no. 1, pp. 1–20, 2008.
- [37] J. J. Dahl and G. E. Trahey, "Off-axis scatterer filters for improved aberration measurements," in *Proc. IEEE Symp. Ultrason.*, vol. 2, Apr. 2003, pp. 1094–1098.
- [38] J. A. Jensen and N. B. Svendsen, "Calculation of pressure fields from arbitrarily shaped, apodized, and excited ultrasound transducers," *IEEE Trans. Ultrason., Ferroelect., Freq. Control*, vol. 39, no. 2, pp. 262–267, Mar. 1992.
- [39] J. A. Jensen, "Field: A program for simulating ultrasound systems," in *Proc. 10th Nordic-Baltic Conf. Biomed. Imag.*, vol. 4, 1996, pp. 351–353.
- [40] R. F. Wagner, S. W. Smith, J. M. Sandrik, and H. Lopez, "Statistics of speckle in ultrasound B-scans," *IEEE Trans. Sonics Ultrason.*, vol. 30, no. 3, pp. 156–163, May 1983.
- [41] C. H. Seo and J. T. Yen, "Evaluating the robustness of dual apodization with cross-correlation," *IEEE Trans. Ultrason., Ferroelect., Freq. Control*, vol. 56, no. 2, pp. 291–303, Feb. 2009.

- [42] B. Byram and J. Shu, "Pseudononlinear ultrasound simulation approach for reverberation clutter," *J. Med. Imag.*, vol. 3, no. 4, p. 046005, 2016.
- [43] B. Byram and J. Shu, "A pseudo non-linear method for fast simulations of ultrasonic reverberation," *Proc. SPIE*, vol. 9790, p. 97900U, Apr. 2016.
- [44] A. Fernandez, J. J. Dahl, D. M. Dumont, and G. E. Trahey, "Aberration measurement and correction with a high resolution 1.75D array," in *Proc. IEEE Ultrason. Symp.*, vol. 2, Apr. 2001, pp. 1489–1494.
- [45] J. C. Laceyfield, W. C. Pilkington, and R. C. Waag, "Distributed aberrators for emulation of ultrasonic pulse distortion by abdominal wall," *Acoust. Res. Lett. Online*, vol. 3, no. 2, pp. 47–52, 2002.
- [46] L. M. Hinkelman, D.-L. Liu, L. A. Metlay, and R. C. Waag, "Measurements of ultrasonic pulse arrival time and energy level variations produced by propagation through abdominal wall," *J. Acoust. Soc. Amer.*, vol. 95, no. 1, pp. 530–541, 1994.
- [47] Y. Sumino and R. C. Waag, "Measurements of ultrasonic pulse arrival time differences produced by abdominal wall specimens," *J. Acoust. Soc. Amer.*, vol. 90, no. 6, pp. 2924–2930, 1991.
- [48] W. F. Walker and G. E. Trahey, "Aberrator integration error in adaptive imaging," *IEEE Trans. Ultrason., Ferroelect., Freq. Control*, vol. 44, no. 4, pp. 780–791, Jul. 1997.



**Kazuyuki Dei** (S'14) was born in Saitama, Japan. He received the B.S. degree in mechanical engineering from the University of California at Berkeley, Berkeley, CA, USA, in 2000. He is currently pursuing the Ph.D. degree in biomedical engineering with Vanderbilt University, Nashville, TN, USA.

He was with Fujitsu Ltd., Tokyo, Japan, and with Fujitsu Semiconductor America Inc., Sunnyvale, CA, USA, as an Electrical Design and Development Engineer over 12 years. His research interests include a model-based clutter suppression, phase-aberration measurements, beamforming, and signal processing.



**Brett Byram** (M'15) received the B.S. degree in biomedical engineering and math from Vanderbilt University, Nashville, TN, USA, in 2004, and the Ph.D. degree in biomedical engineering from Duke University, Durham, NC, USA.

He then stayed as a Research Assistant Professor with Duke University. In 2013, he joined the Biomedical Engineering Department, Vanderbilt University, as an Assistant Professor. He has spent time with the Jørgen Jensen's Center for Fast Ultrasound, Lyngby, Denmark, and also with the Siemens Healthcare's ultrasound Division, Mountain View, CA, USA. He currently runs the Biomedical Elasticity and Acoustic Measurement (BEAM) Laboratory, where he and others with the laboratory pursue solutions to clinical problems using ultrasound. He is also with the Vanderbilt Initiative in Surgery and Engineering and the Vanderbilt University Institute of Imaging Science, Vanderbilt University. His research interests include beamforming, motion estimation, and other related signal processing and hardware development tasks.